



HAL
open science

Fast and slow dynamics in a nonlinear elastic bar excited by longitudinal vibrations

Nicolas Favrie, Bruno Lombard, Cédric Payan

► **To cite this version:**

Nicolas Favrie, Bruno Lombard, Cédric Payan. Fast and slow dynamics in a nonlinear elastic bar excited by longitudinal vibrations. 2014. hal-01041347v1

HAL Id: hal-01041347

<https://hal.science/hal-01041347v1>

Preprint submitted on 23 Jul 2014 (v1), last revised 8 Dec 2014 (v2)

HAL is a multi-disciplinary open access archive for the deposit and dissemination of scientific research documents, whether they are published or not. The documents may come from teaching and research institutions in France or abroad, or from public or private research centers.

L'archive ouverte pluridisciplinaire **HAL**, est destinée au dépôt et à la diffusion de documents scientifiques de niveau recherche, publiés ou non, émanant des établissements d'enseignement et de recherche français ou étrangers, des laboratoires publics ou privés.

Fast and slow dynamics in a nonlinear elastic bar excited by longitudinal vibrations

Nicolas Favrie^a, Bruno Lombard^b, Cédric Payan^b

^aIUSTI, Aix-Marseille Université, UMR CNRS 7343, 5 rue E. Fermi, 13453 Marseille Cedex 13, France

^bLaboratoire de Mécanique et d'Acoustique, UPR 7051 CNRS, 31 chemin Joseph Aiguier, 13402 Marseille, France

Abstract

Heterogeneous materials, such as rocks and concrete, have a complex dynamics including hysteresis, nonlinear elasticity and viscoelasticity. It is very sensitive to microstructural changes and damage. The goal of this paper is to propose a physical model describing the longitudinal vibrations of this class of material, and to develop a numerical strategy for solving the evolution equations. The theory relies on the coupling between two processes with radically-different time scales: a fast process at the frequency of the excitation, governed by nonlinear elasticity and viscoelasticity; a slow process, governed by the evolution of defects. The evolution equations are written as a nonlinear hyperbolic system with relaxation. A time-domain numerical scheme is developed, based on a splitting strategy. The numerical simulations show qualitative agreement with the features observed experimentally by Dynamic Acousto-Elastic Testing.

Keywords: Nonlinear acoustics; time-dependent materials; viscoelasticity; acoustic conditioning; numerical methods; hyperbolic system.

1. Introduction

In geosciences, understanding the complex nonlinear behavior of rocks and soil is valuable for earthquake source characterization, seismic imaging, etc. Within the context on license renewal in nuclear energy, non-destructive evaluation is a key point to evaluate the state of concrete structures, and to estimate the life remaining time. In both cases, many authors report a large, but qualitative, sensitivity of nonlinear parameters to various kinds of damage and pathologies. However, without quantitative data, it is still impossible to compare studies among others.

An unified model describing both nonlinear elasticity and non equilibrium dynamics is of great interest in wave propagation in microheterogeneous media such as rock and concrete. This so-called "non classical" [8, 17, 5] or "mesoscopic" [6] class of material exhibits some nonlinear phenomena unexpected regarding the Landau's theory [9], involving fast and slow dynamic behavior. Fast dynamics describes the quasi-instantaneous nonlinear response of the materials. Slow dynamics relates the slow (order 10^3 s) softening / recovering of the elastic properties when subjected to a high amplitude strain amplitude (order 10^{-6}) dynamic excitation. These

*Corresponding author. Tel.: +33 491 16 44 13.

Email addresses: nicolas.favrie@univ-amu.fr (Nicolas Favrie), lombard@lma.cnrs-mrs.fr (Bruno Lombard), cedric.payan@univ-amu.fr (Cédric Payan)

Preprint submitted to Wave Motion

July 23, 2014

23 phenomena are illustrated in figures 1 and 2. In particular, it is observed experimentally that the
 24 curves relating elastic modulus and strain exhibit hysteresis loops, and vary with the amplitude
 25 of forcing (figure 2).

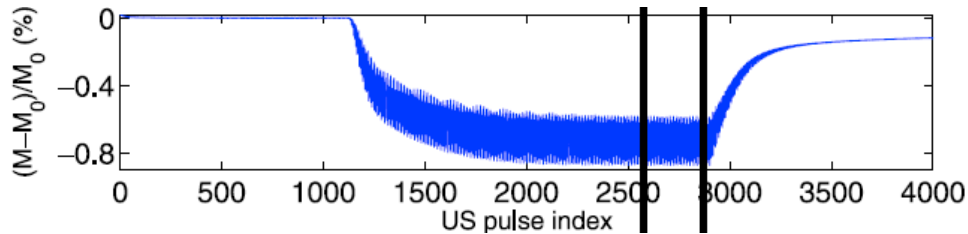


Figure 1: evolution of the relative elastic modulus measured experimentally. Excitation is switched on after 1200 ultrasonic (US) pulses, and then switched off after 2900 US pulses. M and M_0 are the elastic modulus out equilibrium and at equilibrium, respectively. The vertical dotted lines denote a time interval where equilibrium has been reached. Reproduced from figure 3-(a) of [15]. Authorization of reproduction courtesy given by the Authors and by the Journal Editor.

26 The most widely used model describing these behaviors is based on the Preisach-Mayergoyz
 27 theory, introduced in the field of electromagnetism. Even if it can reproduce experimental ob-
 28 servations, this phenomenological model lacks physical foundations. In particular, it does not
 29 incorporate relaxation times [14].

30 Here, we present a "soft-ratchet" model initially introduced in [19] and physically meaning-
 31 full. The softening / recovering of elastic modulus is related to the activation of defects that
 32 evolves dynamically with the applied stress. This relaxation mechanism is coupled to a law of
 33 nonlinear elasticity, for instance the well-known Landau's model [9]. Lastly, viscoelasticity is
 34 introduced in the model. Our contribution is two-fold:

- 35 • Improvement of the physical model. Non-physical features of the soft-ratchet model [19]
 36 are fixed. A generalization of the viscoelastic Zener model to the nonlinear framework is
 37 also introduced. This mechanism of attenuation is more realistic than the Stokes model
 38 used in [19], and is better suited for the numerical resolution.
- 39 • Construction of a numerical scheme. Analytical tools used in [19] were unable to solve
 40 the full coupled system. On the contrary, the numerical strategy developed here enables to
 41 solve the whole equations, in the time-domain.

42 The sketch of the paper is as follows. First, we introduce the physical model and its basic
 43 features in 1D: evolution of defects, nonlinear elasticity, and attenuation. Second, the evolution
 44 equations are written as a first-order system of partial differential equations, whose properties are
 45 stated. Third, the numerical method is introduced, based on a splitting strategy. The hyperbolic
 46 step is solved by a conservative scheme, whereas the relaxation step is solved exactly. Fourth
 47 and last, numerical experiments show that the experimental observations performed by Dynamic
 48 Acousto-Elastic Testing [15, 16] and shown in figures 1 and 2 are qualitatively recovered.

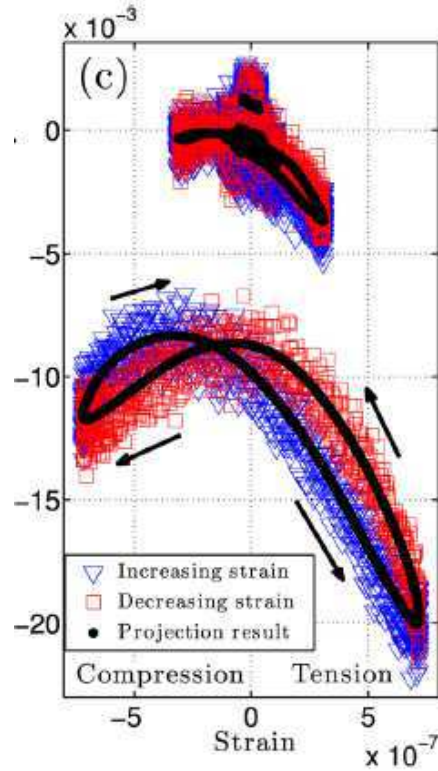


Figure 2: experimental evolution of the elastic modulus in terms of the elastic strain, for various amplitudes of forcing. Reproduced from figure 4-(c) of [16]. Authorization of reproduction courtesy given by the Authors and by the Journal Editor.

49 2. Physical modeling

50 2.1. Linear elastodynamics

In the case of small deformations, the propagation of 1D elastic waves can be described by the following system [1]:

$$\begin{cases} \frac{\partial v}{\partial t} - \frac{1}{\rho} \frac{\partial \sigma}{\partial x} = \gamma, & (1a) \\ \frac{\partial \varepsilon}{\partial t} - \frac{\partial v}{\partial x} = 0, & (1b) \end{cases}$$

51 where t is the time, x is the spatial coordinate, γ is a forcing term, u is the displacement, $v = \frac{\partial u}{\partial t}$ is
 52 the velocity, $\varepsilon = \frac{\partial u}{\partial x}$ is the strain, and σ is the stress. The latter is a function of strain: $\sigma = \sigma(\varepsilon)$.

53 In the linear case, the Hooke's law writes $\sigma = E \varepsilon$, where E is the Young's modulus, which
 54 is assumed to be constant over time. In the particular case where γ is a Dirac source at x_s with

55 time evolution $\mathcal{G}(t)$, then the exact solution of (1) is straightforward

$$\varepsilon = -\frac{\text{sgn}(x - x_s)}{2c^2} \mathcal{G}\left(t - \frac{|x - x_s|}{c}\right), \quad (2)$$

56 where sgn is the sign distribution, and $c = \sqrt{\frac{1}{\rho} \frac{\partial \sigma}{\partial \varepsilon}} \equiv \sqrt{E/\rho}$ is the speed of sound.

57 The goal of the forthcoming sections is to extend the model (1) in three ways:

- 58 • time variations of E due to the stress;
- 59 • nonlinear Hooke's law;
- 60 • hereditary effects (viscoelasticity).

61 The first effect (variation of E) owns time scales much greater than the second and third effect.
62 It is consequently referred to as *slow dynamics*.

63 2.2. *Slow dynamics: soft-ratchet model*

64 Here we follow the lines of [19] with some modifications. The slow dynamics of the medium
65 is assumed to rely on the concentration of activated defects g , which varies with σ . In the lowest
66 approximation, the Young's modulus is written:

$$E = \left(1 - \frac{g}{g_{cr}}\right) E^+, \quad (3)$$

67 where g_{cr} and E^+ are the critical concentration of defects and the maximum possible value of
68 Young's modulus, respectively (figure 3-(a)). The following constraints hold:

$$0 \leq g \leq g_{cr} \leq 1. \quad (4)$$

69 The concentration g is assumed to evolve to its stress-dependent equilibrium value g_σ at a
70 rate f_r if $g > g_\sigma$ (restoration), or f_d if $g < g_\sigma$ (destruction). This mechanism can be modeled by
71 the ordinary differential equation

$$\frac{dg}{dt} = -(f_r H(g - g_\sigma) + f_d H(g_\sigma - g)) (g - g_\sigma), \quad (5)$$

72 where H is the Heaviside step distribution. The frequencies f_r and f_d differ substantially:

$$f_r \ll f_d \ll f_c, \quad (6)$$

73 where f_c is a typical frequency of the excitation. Figure 3-(b) represents the time evolution of
74 g , given a constant equilibrium concentration $g_\sigma = 0.3$ denoted by a horizontal dotted line. The
75 restoration and rapture frequencies are $f_r = 25$ Hz and $f_d = 250$ Hz, respectively. Two initial
76 value of the concentration of defects are considered: $g_0 = 0.2$ and $g_0 = 0.4$. In both cases, g
77 tends towards g_σ with different rates: destruction is much faster than restoration.

78 It remains to define the evolution of g_σ with σ . In [19], the authors propose the expression

$$g_\sigma = g_0 \exp(\sigma/\bar{\sigma}), \quad \bar{\sigma} = \frac{kT}{\nu}, \quad (7)$$

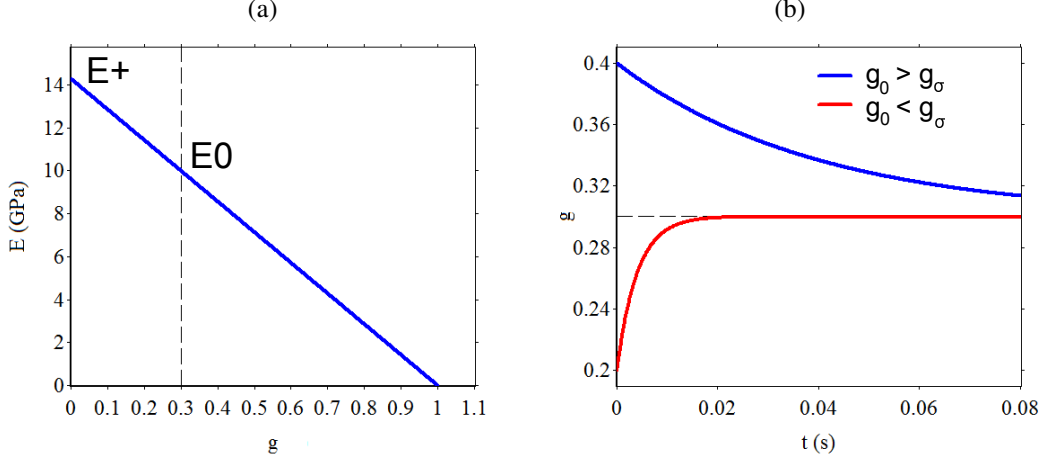


Figure 3: parameters of the slow dynamics. (a): Young's modulus E in terms of the concentration of defects g (3), for $E^+ = 14.28$ GPa; the vertical dotted line denotes the initial concentration of defects $g_0 = 0.3$ and the corresponding Young's modulus $E_0 = E(g_0) = 10$ GPa. (b): time evolution of the concentration of defects g given an equilibrium stress σ and two initial values g_0 ; the horizontal dotted line denotes g_σ .

where g_0 is the unstrained equilibrium concentration of defects, k is the Boltzmann constant, T is the temperature, and ν is a typical volume accounting for a single defect. If $\sigma > \bar{\sigma} \ln g_{cr}/g_0$, then $g_\sigma > g_{cr}$; in this case, the concentration may evolve to $g > g_{cr}$ due to equation (5), which contradicts the second assumption in (4). To remove this drawback and to build a physically realistic expression of g_σ , we enforce (4) together with the following requirements:

$$\begin{cases} 0 \leq g_\sigma < g_{cr}, & (8a) \\ g_\sigma(0) = g_0, & (8b) \\ \lim_{\sigma \rightarrow -\infty} g_\sigma = 0, & (8c) \\ \lim_{\sigma \rightarrow +\infty} g_\sigma = g_{cr}, & (8d) \\ \frac{\partial g_\sigma}{\partial \sigma} > 0. & (8e) \end{cases}$$

79 The simplest smooth function satisfying (8) is

$$g_\sigma = \frac{g_{cr}}{2} \left(1 + \tanh \left(\frac{\sigma - \sigma_0}{\bar{\sigma}} \right) \right), \quad (9)$$

80 where the central stress is

$$\sigma_0 = \bar{\sigma} \tanh^{-1} \left(1 - 2 \frac{g_0}{g_{cr}} \right). \quad (10)$$

81 Figure 4-(a) illustrates the two expressions of the stress-dependent equilibrium value g_σ : the
 82 "exponential model" (7), and the "tanh model" (9)-(10). The numerical values are $g_0 = 0.3$ and
 83 $\bar{\sigma} = 10^5$ Pa. The two expressions are the same at null stress. But for tractions larger than 230 kPa,
 84 the value of g_σ deduced from (7) overcomes 1, leading to non-physical. Figure 4-(b) illustrates

85 the influence of $\bar{\sigma}$ in (9). As $\bar{\sigma}$ decreases, g_{σ} may evolve more easily towards the extreme values
 86 0 and g_{cr} , and hence the damage may increase thanks to (5).

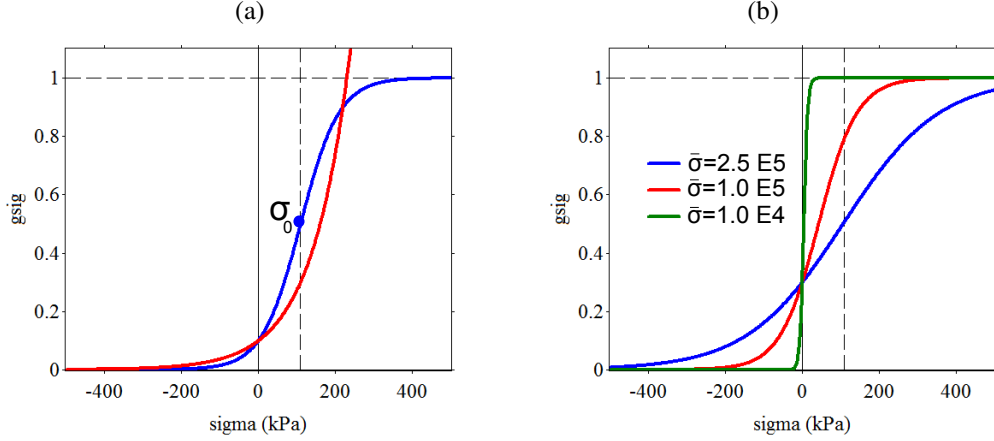


Figure 4: equilibrium concentration of defects g_{σ} in terms of the applied stress σ . (a): "exponential model" (7) and "tanh model" (9). (b): "tanh model" (9) with various values of $\bar{\sigma}$. The horizontal dotted line denotes the critical concentration of defects g_{cr} ; the vertical dotted line denotes the central stress σ_0 .

87 2.3. Fast dynamics: nonlinear viscoelasticity

88 Nonlinear elasticity.

89 The stress-strain relation is given by a smooth function

$$s \equiv s(\epsilon, K, \mathbf{p}), \quad (11)$$

90 where s is the stress, ϵ is the strain, K is a stiffness, and \mathbf{p} is a set of parameters governing the
 91 nonlinearity. No prestress is considered; K is the slope of s at the origin; lastly, s is homogeneous
 92 of degree 1 in K . In other words, s satisfies the following properties:

$$s(0, K, \mathbf{p}) = 0, \quad \frac{\partial s}{\partial \epsilon}(0, K, \mathbf{p}) = K, \quad s(\epsilon, \alpha K, \mathbf{p}) = \alpha s(\epsilon, K, \mathbf{p}). \quad (12)$$

93 Three models of nonlinear elasticity (11) are now given and illustrated in figure 5.

94 **Model 1.** This model is issued from [19] and mimics the Lennard-Jones potential describing the
 95 interaction between a pair of neutral atoms:

$$s(\epsilon, K, \mathbf{p}) = K \frac{d}{r-a} \left(\frac{1}{\left(1 + \frac{\epsilon}{d}\right)^{a+1}} - \frac{1}{\left(1 + \frac{\epsilon}{d}\right)^{r+1}} \right), \quad \mathbf{p} = (r, a, d)^T. \quad (13)$$

96 The nonlinear parameters are the repulsion and attraction coefficients r and a ($0 < a < r$). The
 97 strain is bounded below by the maximal allowable closure d . The function (13) has an extremal
 98 point $\epsilon_c > 0$, and then it decreases asymptotically towards 0 when $\epsilon > \epsilon_c$ (figure 5-(a)).

99 Model 2. A third-order Taylor expansion of the model 1 (13) yields

$$s(\epsilon, K, \mathbf{p}) = K \epsilon \left(1 - \frac{1}{2} (r + a + 3) \frac{\epsilon}{d} + \frac{1}{6} (r^2 + ra + a^2 + 6r + 6a + 11) \left(\frac{\epsilon}{d} \right)^2 \right), \quad \mathbf{p} = (r, a, d)^T. \quad (14)$$

100 The nonlinear parameters are the same than in model 1. But unlike model 1, the function (14)
101 is a strictly monotonic increasing function without extremal point (figure 5-(a)). Moreover, the
102 strain is not bounded below.

103 Model 3. The most widely used law in ultrasonic NonDestructive Testing is the so-called Lan-
104 dau's model [9]

$$s(\epsilon, K, \mathbf{p}) = K \epsilon (1 - \beta \epsilon - \delta \epsilon^2), \quad \mathbf{p} = (\beta, \delta)^T. \quad (15)$$

105 The nonlinear parameters are the quadratic and cubic coefficients β and δ ; in practice, $\beta \ll \delta$.
106 Like model 1, the function (15) has extremal points, but it is not bounded below (figure 5-(b)).

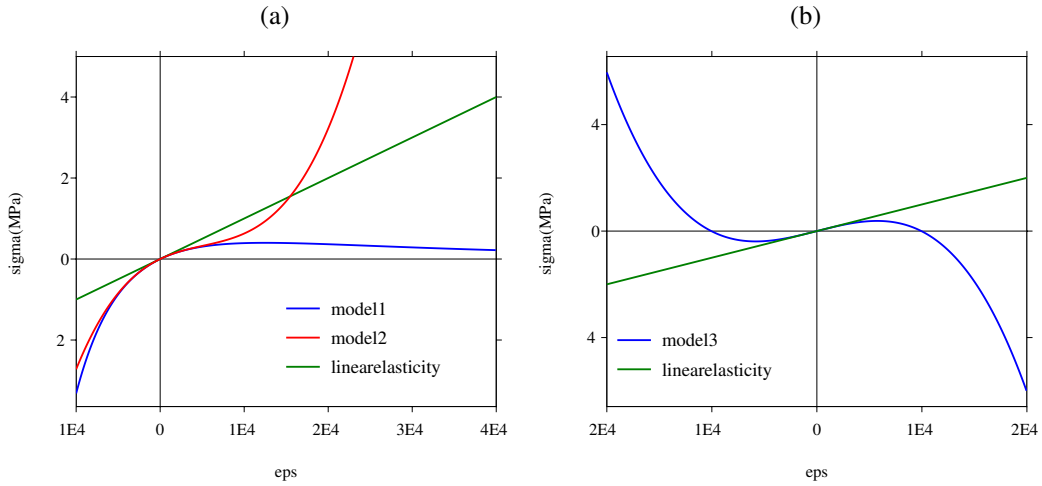


Figure 5: Stress-strain relations for the three models (11). In (a), the dotted lines denote the coordinates of the inflexion point for model 1. The physical parameters are: $E = 10$ GPa, $d = 4.3 \cdot 10^{-4}$ m, $a = 2$, $r = 4$ (models 1 and 2), $\beta = 100$, $\delta = 10^8$ (model 3).

107 *Viscoelasticity.*

108 To incorporate attenuation, the following criteria are used as a guideline:

109 **C₁:** when the viscous effects are null, one must recover the nonlinear elasticity (11);

110 **C₂:** when a linear stress-strain relation holds, one must recover the standard linear solid model
111 (or generalized Zener model), which accurately represents the behavior of usual solids [2].

112 For this purpose, a system with N Zener elements connected in parallel is considered (figure 6).
113 The total stress acting on the system is

$$\sigma = \sum_{\ell=1}^N \sigma_{1\ell} = \sum_{\ell=1}^N (\sigma_{2\ell} + \sigma_{3\ell}), \quad (16)$$

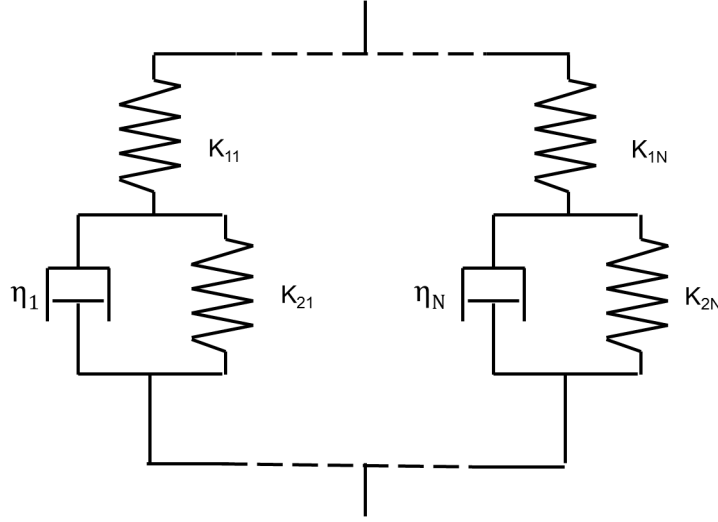


Figure 6: Rheological model of a generalized Zener material.

114 where the index 1 refers to the series springs, and the indices 2-3 refer to the springs and dashpots
 115 in parallel. The strain ε is

$$\varepsilon = \varepsilon_{1\ell} + \varepsilon_{2\ell}, \quad \ell = 1, \dots, N. \quad (17)$$

The springs 1 satisfy nonlinear stress-strain relations (11) with stiffnesses $K_{1\ell}$. The parameters \mathbf{p} governing the nonlinearity (for instance β and δ in model 3 (15)) are assumed to be constant and identical for each element. The springs 2 satisfy linear stress-strain relations with stiffnesses $K_{2\ell}$. Lastly, the dashpots satisfy linear Maxwell laws with coefficients of viscosity η_ℓ . These laws are summed up as follows:

$$\begin{cases} \sigma_{1\ell}(\varepsilon_{1\ell}) = s(\varepsilon_{1\ell}, K_{1\ell}, \mathbf{p}), & (18a) \\ \sigma_{2\ell}(\varepsilon_{2\ell}) = s(\varepsilon_{2\ell}, K_{2\ell}, \mathbf{0}), & (18b) \\ \sigma_{3\ell}(\varepsilon_{2\ell}) = \eta_\ell \frac{\partial \varepsilon_{2\ell}}{\partial t}. & (18c) \end{cases}$$

116 To determine the parameters $K_{1\ell}$, $K_{2\ell}$ and η_ℓ , one introduces the relaxation times $\tau_{\sigma\ell}$, $\tau_{\varepsilon\ell}$ and the
 117 relaxed modulus E_R :

$$\tau_{\sigma\ell} = \frac{\eta_\ell}{K_{1\ell} + K_{2\ell}}, \quad \tau_{\varepsilon\ell} = \frac{\eta_\ell}{K_{2\ell}}, \quad \frac{E_R}{N} = \frac{K_{1\ell} K_{2\ell}}{K_{1\ell} + K_{2\ell}}. \quad (19)$$

118 On one hand, a procedure is given in Appendix A to compute the relaxation times in terms of the
 119 quality factor Q . On the other hand, E_R is related to the unrelaxed Young's modulus E (3) and to
 120 the relaxation times previously determined (see [2]):

$$E_R = \frac{N}{\sum_{\ell=1}^N \frac{\tau_{\varepsilon\ell}}{\tau_{\sigma\ell}}} E. \quad (20)$$

121 Once $\tau_{\sigma\ell}$, $\tau_{\varepsilon\ell}$ and E_R are determined, inverting (19) provides the values of the viscoelastic model
 122 in terms of the relaxed modulus and relaxation times ($\ell = 1, \dots, N$):

$$K_{1\ell} = \frac{\tau_{\varepsilon\ell}}{\tau_{\sigma\ell}} \frac{E_R}{N}, \quad K_{2\ell} = \frac{\tau_{\varepsilon\ell}}{\tau_{\varepsilon\ell} - \tau_{\sigma\ell}} \frac{E_R}{N}, \quad \eta_\ell = \frac{\tau_{\varepsilon\ell}^2}{\tau_{\varepsilon\ell} - \tau_{\sigma\ell}} \frac{E_R}{N}. \quad (21)$$

123 From (20) and (21), it follows that the viscoelastic parameters depend indirectly on the Young's
 124 modulus E , and thus depend on g . In other words, the proposed model of viscoelasticity evolves
 125 with the concentration of defects and thus with the applied stress.

126 To conclude this part, let us recall the two criteria C_1 and C_2 used to build the viscoelastic
 127 model. C_1 concerned the consistency with the Zener model in the linear case, whereas C_2 concerned
 128 the consistency with the nonlinear elasticity (11) in the inviscid case. By construction, C_1
 129 is satisfied. The following property states that C_2 is also true. The proof is given in Appendix A.

130 **Property 1.** *In the inviscid case, the stress-strain relation deduced from (16)-(18) recovers the*
 131 *nonlinear elasticity (11), whatever the number N of relaxation mechanisms.*

132 3. Mathematical modeling

133 3.1. First-order system

134 The conservation of momentum (1a) writes

$$\frac{\partial v}{\partial t} = \frac{1}{\rho} \frac{\partial \sigma}{\partial x} + \gamma, \quad (22)$$

135 where γ is a forcing term, and σ is given by (16). The hypothesis of small deformations (1b)
 136 gives

$$\frac{\partial \varepsilon}{\partial t} = \frac{\partial v}{\partial x}. \quad (23)$$

137 Lastly, manipulations on (16), (17) and (18c) yield

$$\frac{\partial \varepsilon_{1\ell}}{\partial t} = \frac{\partial v}{\partial x} + \frac{\sigma_{2\ell}(\varepsilon - \varepsilon_{1\ell}) - \sigma_{1\ell}(\varepsilon_{1\ell})}{\eta_\ell}, \quad \ell = 1, \dots, N. \quad (24)$$

In (24), $\varepsilon_{1\ell}$ takes the place of the memory variables proposed in [12] and is better suited to
 nonlinear elasticity. Putting together (22)-(24) and the relaxation equation (5) leads to the first-
 order system of $N + 3$ evolution equations

$$\left\{ \begin{array}{l} \frac{\partial v}{\partial t} - \frac{1}{\rho} \frac{\partial \sigma}{\partial x} = \gamma, \end{array} \right. \quad (25a)$$

$$\left\{ \begin{array}{l} \frac{\partial \varepsilon}{\partial t} - \frac{\partial v}{\partial x} = 0, \end{array} \right. \quad (25b)$$

$$\left\{ \begin{array}{l} \frac{\partial \varepsilon_{1\ell}}{\partial t} - \frac{\partial v}{\partial x} = \frac{\sigma_{2\ell}(\varepsilon - \varepsilon_{1\ell}) - \sigma_{1\ell}(\varepsilon_{1\ell})}{\eta_\ell}, \quad \ell = 1, \dots, N, \end{array} \right. \quad (25c)$$

$$\left\{ \begin{array}{l} \frac{dg}{dt} = -(f_r H(g - g_\sigma) + f_d H(g_\sigma - g)) (g - g_\sigma). \end{array} \right. \quad (25d)$$

138 To close the system (25), one recalls the following equations:

- 139 • The total stress σ in (25a) depends on $\varepsilon_{1\ell}$ via (16), (18a), and a nonlinear law (11):

$$\sigma = \sum_{\ell=1}^N s(\varepsilon_{1\ell}, K_{1\ell}, \mathbf{p}). \quad (26)$$

- 140 • The stress components $\sigma_{1\ell}$ and $\sigma_{2\ell}$ in (25c) depend on the stiffnesses $K_{1\ell}$ and $K_{2\ell}$ (18a) and
141 (18b). The latter, as well as the viscosities coefficients η_ℓ , depend on the Young modulus
142 E via (20)-(21), and thus on g :

$$E = \left(1 - \frac{g}{g_{cr}}\right) E^+. \quad (27)$$

- 143 • The equilibrium value of the defect concentration g_σ in (25d) satisfies (9) and (10):

$$g_\sigma = \frac{g_{cr}}{2} \left(1 + \tanh\left(\frac{\sigma - \sigma_0}{\bar{\sigma}}\right)\right). \quad (28)$$

144 The system (25) together with equations (26)-(28) generalizes the standard equations of linear
145 elastodynamics (1). It accounts for softening / recovering of Young's modulus, nonlinearity and
146 viscoelasticity.

147 For the sake of clarity, one introduces the vector of $N + 3$ unknowns

$$\mathbf{U} = (v, \varepsilon, \varepsilon_{11}, \dots, \varepsilon_{1N}, g)^T. \quad (29)$$

148 Then the system (25) can be put in the form

$$\frac{\partial}{\partial t} \mathbf{U} + \frac{\partial}{\partial x} \mathbf{F}(\mathbf{U}) = \mathbf{R}(\mathbf{U}) + \mathbf{\Gamma}. \quad (30)$$

149 The flux function \mathbf{F} , the relaxation term \mathbf{R} , and the forcing \mathbf{S} are

$$\begin{aligned} \mathbf{F}(\mathbf{U}) &= \left(-\frac{\sigma}{\rho}, -v, -v, \dots, -v, 0\right)^T, \\ \mathbf{R}(\mathbf{U}) &= (0, 0, \Delta_1, \dots, \Delta_N, -(f_r H(g - g_\sigma) + f_d H(g_\sigma - g)) (g - g_\sigma))^T, \\ \mathbf{\Gamma} &= (\gamma, 0, \dots, 0, 0)^T, \end{aligned} \quad (31)$$

150 where

$$\Delta_\ell = \frac{\sigma_{2\ell}(\varepsilon - \varepsilon_{1\ell}) - \sigma_{1\ell}(\varepsilon_{1\ell})}{\eta_\ell}. \quad (32)$$

151 To conclude, let us consider the limit-case where the viscoelastic attenuation is neglected. In
152 this case, property 1 states that the stress-strain relations degenerate rigorously towards pure
153 nonlinear elasticity, whatever N . But for computational purpose, it is more efficient to eliminate
154 the additional strain variables $\varepsilon_{1\ell}$ and the equation (25c). A reduced system (30) is therefore
155 obtained.

156 **3.2. Properties**

157 Hyperbolicity is a crucial issue in wave problems, both physically and mathematically. It
 158 amounts to say that there exists a real and finite sound velocity c . This property has been analysed
 159 in [13] for a particular nonlinear stress-strain relation in 3D. In 1D, it reduces to a simpler case
 160 detailed as follows.

161 **Property 2.** *Let define the sound speed c by*

$$c^2 = \sum_{\ell=1}^N c_\ell^2 = \frac{1}{\rho} \sum_{\ell=1}^N \frac{\partial \sigma_{1\ell}}{\partial \varepsilon_{1\ell}}. \quad (33)$$

162 *The system (30) is hyperbolic if and only if $c^2 > 0$ in (33).*

163 The proof is given in Appendix B. Necessary and sufficient conditions are easily deduced
 164 from (33) for the models (13)-(15) when $N = 1$: hyperbolicity is satisfied if $|\varepsilon| < \varepsilon_c$, where

$$\varepsilon_c = \begin{cases} d \left(\left(\frac{r+1}{a+1} \right)^{\frac{1}{r-a}} - 1 \right) & \text{(model 1),} \\ +\infty & \text{(model 2),} \\ \frac{1}{2\beta} \text{ if } \delta = 0, \quad \frac{\beta}{3\delta} \left(\sqrt{1 + \frac{3\delta}{\beta^2}} - 1 \right) \text{ otherwise} & \text{(model 3).} \end{cases} \quad (34)$$

165 Model 2 is always hyperbolic. On the contrary, the widely-used Landau model (model 3) is
 166 conditionally hyperbolic. When $N > 1$, the hyperbolicity condition $|\varepsilon_{1\ell}| < \varepsilon_c$ is sufficient.

167 Expressions of the sound speed c for the three nonlinear elastic models (13)-(15) are given in
 168 (B.5). From (33), one deduces the local elastic modulus M

$$M = \rho c^2 = \sum_{\ell=1}^N \frac{\partial \sigma_{1\ell}}{\partial \varepsilon_{1\ell}}. \quad (35)$$

169 To conclude on hyperbolicity, let us note that the Stokes viscoelastic model used in [19] intro-
 170 duces a term $\frac{\partial^2 v}{\partial x^2}$ in the right-hand side of (25c). This Laplacian term destroys the hyperbolic
 171 character of the system (30). The viscoelastic model used here has therefore better mathematical
 172 properties.

173 Now we examine the spectrum of the relaxation function in (30). Some useful insight can be
 174 obtained in the case of small strains.

175 **Property 3.** *Let us consider linear stress-strain relations. The parameters $K_{1\ell}$, $K_{2\ell}$ and η_ℓ are*
 176 *"frozen" in (20)-(21), so that they do not depend on g via E (3). Then, the eigenvalues of the*
 177 *Jacobian matrix $\mathbf{J} = \frac{\partial \mathbf{R}}{\partial \mathbf{U}}$ are*

$$\text{Sp}(\mathbf{J}) = \left\{ 0^2, -f_\xi, -\frac{K_{1\ell} + K_{2\ell}}{\eta_\ell} \right\} = \left\{ 0^2, -f_\xi, -\frac{1}{\tau_{\sigma\ell}} \right\}, \quad \ell = 1, \dots, N, \quad (36)$$

178 (see (19)), with $f_\xi = f_r$ if $g > g_\sigma$, $f_\xi = f_d$ if $g < g_\sigma$, $f_\xi = 0$ else.

179 The proof of property 3 is detailed in Appendix C. Two remarks are deduced:

- 180 • \mathbf{J} is definite-negative if the relaxation frequencies $\tau_{\sigma\ell}$ are positive. The latter parameters
181 are deduced from an optimization process based on the quality factor (Appendix A). To
182 ensure the energy decrease, it is therefore crucial to perform nonlinear optimization with
183 constraint of positivity.
- 184 • The optimization procedure detailed in Appendix A is performed on the frequency range
185 $[f_{\min}, f_{\max}]$ surrounding the excitation frequency f_c . These frequencies satisfy

$$f_{\min} \approx \frac{1}{\max \tau_{\sigma\ell}} < f_c < f_{\max} \approx \frac{1}{\min \tau_{\sigma\ell}}. \quad (37)$$

186 In (37), \approx are replaced by equalities if a linear optimisation is used [12]. From (6), it
187 follows the spectral radius of \mathbf{J}

$$\varrho(\mathbf{J}) = \frac{1}{\min \tau_{\sigma\ell}} \gg f_{\xi}, \quad (38)$$

188 so that the system (30) is stiff.

189 4. Numerical modeling

190 4.1. Splitting

191 To integrate (30), one introduces a uniform spatial mesh Δx and a variable time step $\Delta t^{(n)} \equiv$
192 Δt . One seeks an approximation \mathbf{U}_i^n of the exact solution $\mathbf{U}(x_i = i \Delta x, t_n = t_{n-1} + \Delta t)$. A first
193 strategy is to discretize explicitly the non-homogeneous system (30). But numerical stability
194 implies a bound of the form

$$\Delta t \leq \min \left(\frac{\Delta x}{c_{\max}}, \frac{2}{\varrho(\mathbf{J})} \right), \quad (39)$$

195 where $c_{\max} = \max c_i^n$ is the maximal sound velocity at time t_n , and $\varrho(\mathbf{J})$ is the spectral radius of
196 the Jacobian of the relaxation term. As deduced from (38), the second bound in (39) is penalizing
197 compared with the standard CFL condition $\Delta t \leq \Delta x / c_{\max}$.

198 Here we follow another strategy: equation (30) is split into a hyperbolic step

$$\frac{\partial}{\partial t} \mathbf{U} + \frac{\partial}{\partial x} \mathbf{F}(\mathbf{U}) = \mathbf{0} \quad (40)$$

199 and a relaxation step

$$\frac{\partial}{\partial t} \mathbf{U} = \mathbf{R}(\mathbf{U}) + \mathbf{\Gamma}. \quad (41)$$

The discrete operators associated with the discretization of (40) and (41) are denoted \mathbf{H}_h and \mathbf{H}_r ,
respectively. The second-order Strang splitting is used, solving successively (40) and (41) with
adequate time increments:

$$\left\{ \begin{array}{l} \mathbf{U}_i^{(1)} = \mathbf{H}_r \left(\frac{\Delta t}{2} \right) \mathbf{U}_i^n, \\ \mathbf{U}_i^{(2)} = \mathbf{H}_h (\Delta t) \mathbf{U}_i^{(1)}, \\ \mathbf{U}_i^{n+1} = \mathbf{H}_r \left(\frac{\Delta t}{2} \right) \mathbf{U}_i^{(2)}. \end{array} \right. \quad \begin{array}{l} (42a) \\ (42b) \\ (42c) \end{array}$$

200 Provided that \mathbf{H}_h and \mathbf{H}_r are second-order accurate and stable operators, the time-marching (42)
 201 gives a second-order accurate approximation of the original equation (30) [10].

202 4.2. Hyperbolic step

203 The homogeneous equation (40) is solved by a conservative scheme for hyperbolic systems
 204 [10]

$$\mathbf{U}_i^{n+1} = \mathbf{U}_i^n - \frac{\Delta t}{\Delta x} (\mathbf{F}_{i+1/2} - \mathbf{F}_{i-1/2}). \quad (43)$$

205 Many sophisticated schemes can be used for this purpose [11]. For the sake of simplicity and
 206 robustness, we use here the Godunov scheme. Its numerical flux function $\mathbf{F}_{i+1/2}$ is computed by
 207 the Rusanov method [18]

$$\mathbf{F}_{i+1/2} = \frac{1}{2} (\mathbf{F}(\mathbf{U}_{i+1}^n) + \mathbf{F}(\mathbf{U}_i^n) - \lambda_{i+1/2} (\mathbf{U}_{i+1}^n - \mathbf{U}_i^n)), \quad (44)$$

208 where \mathbf{f} is the flux function (31), and the diffusion parameter $\lambda_{i+1/2}$ is given by the Davis approx-
 209 imation [4]

$$\lambda_{i+1/2} = \max(c_i^n, c_{i+1}^n). \quad (45)$$

210 The Godunov scheme is first-order accurate and stable under the usual CFL condition

$$\Delta t = \frac{\alpha \Delta x}{c_{\max}}, \quad \text{with } \alpha \leq 1. \quad (46)$$

211 4.3. Relaxation step

Let us denote $\bar{\mathbf{U}} = (\varepsilon, \varepsilon_{11}, \dots, \varepsilon_{1N})$ and $\bar{\mathbf{R}}$ the restriction of $\mathbf{R}(\mathbf{U})$ to the strain components
 (31)-(32). The ordinary differential equation (41) can then be written

$$\begin{cases} \frac{\partial v}{\partial t} = \gamma, & (47a) \\ \frac{\partial \bar{\mathbf{U}}}{\partial t} = \bar{\mathbf{R}}(\bar{\mathbf{U}}), & (47b) \\ \frac{dg}{dt} = -(f_r H(g - g_\sigma) + f_d H(g_\sigma - g)) (g - g_\sigma), & (47c) \end{cases}$$

212 The viscoelastic parameters in the relaxation function $\bar{\mathbf{R}}$ depend implicitly on g (see section 2.3),
 213 which complicates the resolution of (47a). However, one can take advantage of the scaling (6).
 214 Indeed, ε and $\varepsilon_{1\ell}$ evolve much faster than g , so that the viscoelastic parameters $K_{1\ell}$, $K_{2\ell}$, η_ℓ are
 215 almost constant on a time step. Consequently, they are frozen and the three equations in (47)
 216 can be solved separately.

217 The half-time step in the relaxation steps (42a)-(42c) is denoted by $\tau = \frac{\Delta t}{2}$. One details the
 218 time-stepping from t_n to the first intermediate step (42a); adaptation to the third intermediate step
 219 (42c) is straightforward.

220 The first equation (47a) is integrated by the Euler method:

$$v_i^{n+1} = v_i^{(1)} + \Delta t \gamma(i, t_n). \quad (48)$$

221 To integrate the second equation (47b), a first-order Taylor expansion of $\overline{\mathbf{R}}(\overline{\mathbf{U}})$ is performed

$$\frac{\partial}{\partial t} \overline{\mathbf{U}} \approx \overline{\mathbf{R}}(\overline{\mathbf{0}}) + \frac{\partial \overline{\mathbf{R}}}{\partial \overline{\mathbf{U}}}(\overline{\mathbf{0}}) \overline{\mathbf{U}} = \overline{\mathbf{J}} \overline{\mathbf{U}}, \quad (49)$$

222 where $\overline{\mathbf{J}}$ is the Jacobian matrix (C.2); the nullity of stress at zero strain has been used (18a). Then
223 (49) is solved exactly, leading to the relaxation operator

$$\overline{\mathbf{U}}_i^{(1)} = e^{\overline{\mathbf{J}} \tau} \overline{\mathbf{U}}_i^n \quad (50)$$

224 with the exponential of matrix

$$e^{\overline{\mathbf{J}} \tau} = \begin{pmatrix} 1 & 0 & \dots & 0 \\ \frac{E_{21}}{E_{11} + E_{21}} \left(1 - e^{-\frac{E_{11} + E_{21}}{\eta_1} \tau}\right) & e^{-\frac{E_{11} + E_{21}}{\eta_1} \tau} & & \\ \vdots & & \ddots & \\ \frac{E_{2N}}{E_{1N} + E_{2N}} \left(1 - e^{-\frac{E_{1N} + E_{2N}}{\eta_N} \tau}\right) & & & e^{-\frac{E_{1N} + E_{2N}}{\eta_N} \tau} \end{pmatrix}. \quad (51)$$

225 Lastly, the third equation (47c) is solved exactly. The grid value $g_{\sigma i}$ is evaluated thanks to (9).
226 Setting

$$f_{\xi} = \begin{cases} f_r & \text{if } g_i^n \geq g_{\sigma i}^n, \\ f_d & \text{if } g_i^n < g_{\sigma i}^n, \end{cases} \quad (52)$$

227 one obtains

$$g_i^{(1)} = g_{\sigma i}^n + (g_i^n - g_{\sigma i}^n) e^{-f_{\xi} \tau}. \quad (53)$$

228 The integrations (50), (48) and (53) are unconditionally stable. As a consequence, the splitting
229 (42) is stable under the CFL condition (46).

230 4.4. Summary of the algorithm

231 The numerical method can be divided in two parts:

232 1. initialisation

- 233 • bulk modulus ρ , Young's modulus $E = E_0 = \rho c_{\infty}^2$;
- 234 • soft-ratchet coefficients $g_{cr} = 1$, $g = g_0$, f_r , f_d , $\overline{\sigma}$;
- 235 • maximum Young's modulus E^+ (3)
- 236 • nonlinear coefficients (e.g. β and δ in (15));
- 237 • quality factor Q , frequency range of optimization $[f_{\min}, f_{\max}]$, number of relaxation
238 mechanisms N ;
- 239 • optimization of the viscoelastic coefficients (Appendix A);

240 2. time-marching $t_n \rightarrow t_{n+1}$, $x_i = i \Delta x$ ($n = 0, \dots, N_t$, $i = 1, \dots, N_x$)

- 241 • physical and numerical parameters
- 242 - Young's modulus E (3), viscoelastic parameters E_R (20), $K_{1\ell}$, $K_{2\ell}$ and η_{ℓ} (21);
- 243 - stresses $\sigma_{1\ell}$ (18a) and σ (16);

- 244 - sound velocity c (33) and (B.5), maximal velocity c_{\max} ;
- 245 - time step Δt (46);
- 246 • relaxation step \mathbf{H}_r (42a)
 - 247 - strains (50) and (51);
 - 248 - elastic velocity v (48);
 - 249 - concentration of defects g_σ (9), g (53);
- 250 • hyperbolic step \mathbf{H}_h (42b)
 - 251 - coefficient $\lambda_{i+1/2}$ of Davis (45);
 - 252 - computation of the flux \mathbf{F} (31) e.g. by the Rusanov flux $\mathbf{F}_{i+1/2}$ (44);
 - 253 - time-marching with the conservative scheme (43);
- 254 • relaxation step \mathbf{H}_r (42c).

255 5. Numerical experiments

256 5.1. Configuration

ρ (kg/m ³)	E_0 (GPa)	g_0	f_r (Hz)	f_d (Hz)	$\bar{\sigma}$ (GPa)	β	δ	Q
2054	2.21	0.1	25	250	0.1	40	$3.5 \cdot 10^6$	20

Table 1: Physical parameters.

257 The physical parameters are detailed in table 1. Depending on the test, some of these para-
258 meters are modified. In the limit-case of linear elasticity, the sound velocity is $c = \sqrt{E/\rho} = 3280$
259 m/s. The maximal CFL number is $\alpha = 0.95$ in (46). The mesh size is $\Delta x = 4 \cdot 10^{-3}$ m. Depending
260 on the test, two lengths of domain are considered. For each test, a receiver put at $x_r = 0.2$ m
261 stores the numerical solution at each time step.

262 The wave fields are excited by a punctual source at $x_s = 10^{-2}$ m, with a central frequency
263 $f_c = 10$ kHz. Depending on the expression of the forcing γ in (25c), one deduces the magnitude
264 of the maximal strain ε_{\max} emitted by the source in the limit-case of linear elasticity (2):

$$\varepsilon_{\max} = \frac{1}{2c^2} \max \mathcal{G}(t). \quad (54)$$

265 The Landau model for nonlinear elasticity is used (15). The quadratic coefficient β is much
266 smaller than the cubic one δ . The critical value of strain that ensures hyperbolicity (34) is $\varepsilon_c =$
267 $3.08 \cdot 10^{-4}$. The viscoelastic effects are described by $N = 4$ relaxation mechanisms. The relaxation
268 times $\tau_{\sigma\ell}$ and $\tau_{\varepsilon\ell}$ (19) are computed by optimization on the frequency range [$f_{\min} = f_c/10$, $f_{\max} =$
269 $f_c \times 10$] (see Appendix A); they are given in table 2.

	$\ell = 1$	$\ell = 2$	$\ell = 3$	$\ell = 4$
$\tau_{\sigma\ell}$ (s)	$1.16 \cdot 10^{-3}$	$2.05 \cdot 10^{-4}$	$4.49 \cdot 10^{-5}$	$7.75 \cdot 10^{-6}$
$\tau_{\varepsilon\ell}$ (s)	$1.53 \cdot 10^{-3}$	$2.49 \cdot 10^{-4}$	$5.50 \cdot 10^{-5}$	$1.06 \cdot 10^{-5}$

Table 2: Relaxation times for a quality factor $Q = 20$. Optimization with $N = 4$ relaxation mechanisms on the frequency range [1 kHz, 100 kHz].

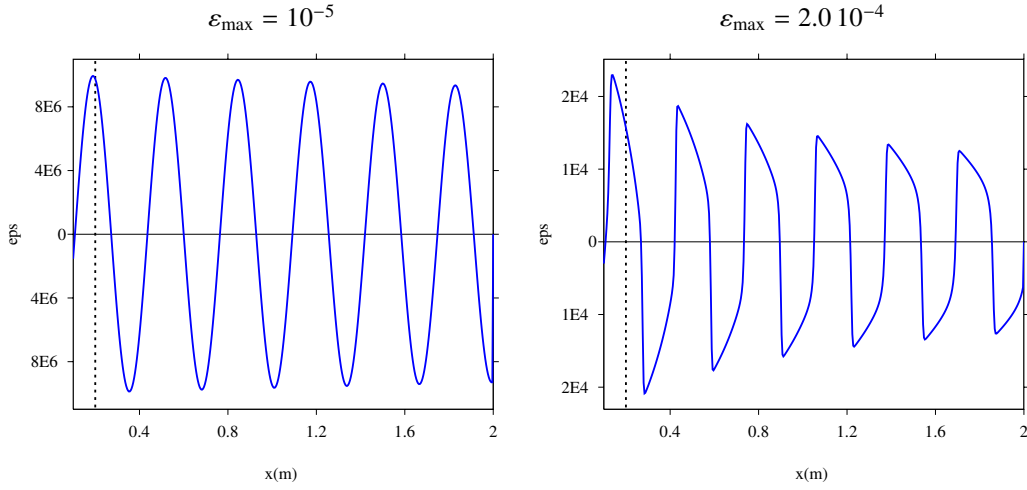


Figure 7: test 1. Snapshot of the strain after 400 time steps, for two amplitudes of the excitation. The vertical dotted line denotes the location x_r of the receiver.

270 5.2. Test 1: nonlinear elastodynamics

271 The goal of the first test is to show typical features of wave propagation in purely nonlin-
 272 ear elastic media. The viscoelasticity is neglected, and the activation / restoration of defects is
 273 annihilated: $f_r = f_d = 0$ Hz. The source is a monochromatic excitation:

$$\mathcal{G}(t) = A \sin(\omega_c t) H(t), \quad (55)$$

274 where A is the magnitude of the forcing, and $\omega_c = 2\pi f_c$. From (54) and (55), one can esti-
 275 mate the maximal strain ε_{\max} emitted by the source in the linear elastic case. The domain of
 276 propagation is $L_x = 2$ m long and is discretized onto 400 grid nodes.

277 Figure 7 displays the spatial evolution of ε after 400 time steps. For $\varepsilon_{\max} = 10^{-5}$, almost no
 278 distortion of the wave is seen. On the contrary, $\varepsilon_{\max} = 2.0 \cdot 10^{-4}$ yields a high distortion as wave
 279 propagates. Shocks are observed, as well as the attenuation due to the decrease of entropy.

280 Figure 8 displays the time evolution of the strain recorded at the receiver (vertical dotted line
 281 in Figure 7) for $\varepsilon_{\max} = 2.0 \cdot 10^{-4}$. The normalized amplitudes of the Fourier series decomposition
 282 show a typical feature of cubic nonlinear elasticity: the spectrum involves mainly odd harmonics
 283 [7].

284 5.3. Test 2: linear viscoelasticity

The goal of the second test is to validate the numerical modeling of attenuation. For this
 purpose, a linear stress-strain relation is chosen ($\beta = \delta = 0$), and the activation / restoration of

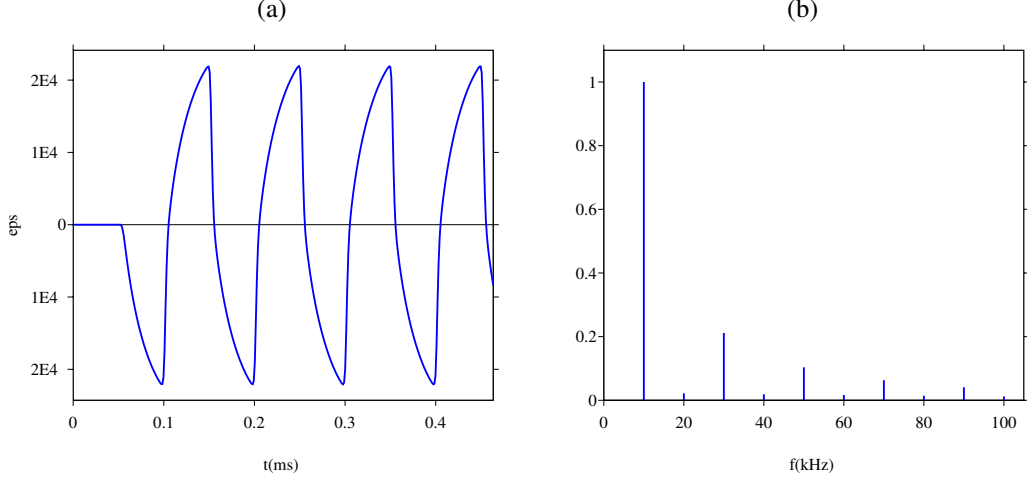


Figure 8: test 1. Time history of the strain at the receiver at x_r (a), normalized Fourier coefficients (b). The amplitude of the excitation is $\epsilon_{\max} = 2.0 \cdot 10^{-4}$.

defects is still annihilated ($f_r = f_d = 0$ Hz). Consequently, the system (25) simplifies into

$$\begin{cases} \frac{\partial v}{\partial t} - \frac{1}{\rho} \frac{\partial \sigma}{\partial x} = \gamma, & (56a) \end{cases}$$

$$\begin{cases} \frac{\partial \epsilon}{\partial t} - \frac{\partial v}{\partial x} = 0, & (56b) \end{cases}$$

$$\begin{cases} \frac{\partial \epsilon_{1\ell}}{\partial t} - \frac{\partial v}{\partial x} = \frac{K_{2\ell}}{\eta_\ell} (\epsilon - \epsilon_{1\ell}) - \frac{K_{1\ell}}{\eta_\ell} \epsilon_{1\ell}. & (56c) \end{cases}$$

285 The domain of propagation is $L_x = 2$ m long and is discretized onto 400 grid nodes. The time
286 evolution of the source is a truncated combination of sinusoids with C^6 smoothness:

$$\mathcal{G}(t) = \begin{cases} \sum_{m=1}^4 a_m \sin(b_m \omega_c t) & \text{if } 0 \leq t \leq \frac{1}{f_c}, \\ 0 & \text{otherwise,} \end{cases} \quad (57)$$

287 with parameters $b_m = 2^{m-1}$, $a_1 = 1$, $a_2 = -21/32$, $a_3 = 63/768$ and $a_4 = -1/512$. A set of 5
288 receivers is put at abscissae $x_r = 0.5 + 0.3(j-1)$, with $j = 1, \dots, 5$.

289 Figure 9-(a) shows a seismogram of the velocity recorded at the receivers. Attenuation and
290 dispersion of the waves is clearly observed. Figure 9-(b) compares the numerical solution with
291 the semi-analytical solution after 400 time steps. The computation of the semi-analytical solution
292 is described in Appendix D; it is numerically evaluated with $N_f = 512$ Fourier modes, with a
293 frequency step $\Delta f = 200$ Hz. Good agreement is observed between numerical and exact values.
294 The attenuation is slightly overestimated by the scheme, due to the numerical diffusion of the
295 Godunov scheme [18].

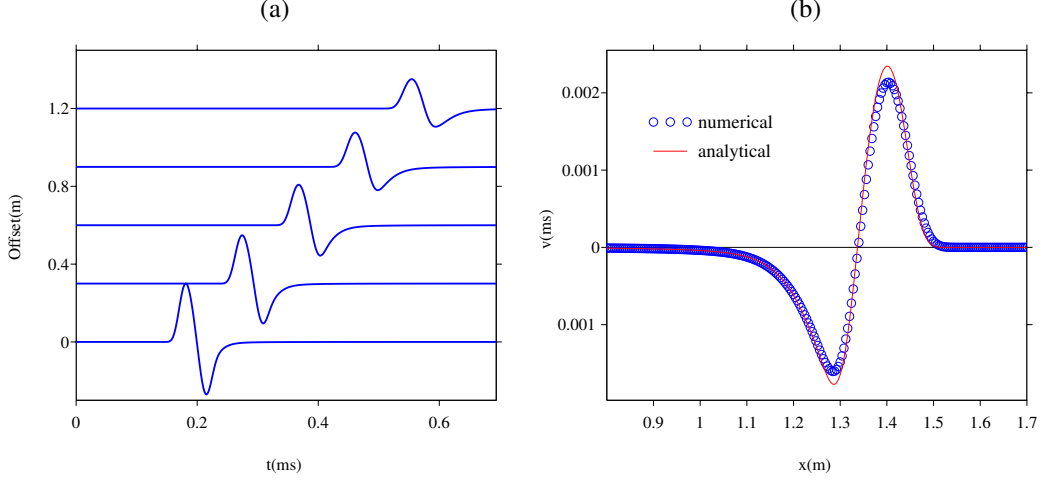


Figure 9: test 2. Wave propagation in a viscoelastic medium. (a): time evolution of v at a set of receivers; (b): snapshot of v at $t = 0.46$ ms, and comparison between the numerical and the semi-analytical solution.

296 5.4. Test 3: softening / recovering

297 The goal of the third test is to illustrate the softening / recovering of the elastic modulus,
 298 and to validate the numerical modeling of this phenomenon. For this purpose, linear elasticity
 299 is assumed and viscoelasticity is neglected ($\beta = \delta = 0$, $Q = +\infty$). Even if a linear stress-strain
 300 relation is used, the evolution problem (25) is nonlinear by virtue of (25d), (27) and (28). As in
 301 test 1, the source is monochromatic; but it is switched off after a time t^* :

$$\mathcal{G}(t) = A \sin(\omega_c t) (H(t) - H(t^*)). \quad (58)$$

302 As long as the source is switched on ($0 < t < t^*$), the equilibrium concentration of defects
 303 increases from the initial value g_0 up to $g^* = g(t^*)$. In the same time, the Young's modulus
 304 decreases from E_0 to E^* via (3).

305 For $t > t^*$, the waves go out of the domain, and the elastodynamic fields vanish. From (28)
 306 and (10), $\sigma = 0$ implies that the equilibrium concentration of defects becomes $g_\sigma = g_0$. As a
 307 consequence, the ODE (25d) describing the evolution of defects simplifies into

$$\begin{cases} \frac{dg}{dt} = -f_r (g - g_0), \\ g(t^*) = g^*. \end{cases} \quad (59)$$

308 The solution of (59) is

$$g(t) = g_0 + (g^* - g_0) e^{-f_r(t-t^*)}. \quad (60)$$

309 Equation (60) is injected into (3), which gives the time evolution of the Young's modulus during
 310 the recovering process ($t \geq t^*$):

$$E(t) = E_0 - \frac{1}{g_{cr}} (g^* - g_0) e^{-f_r(t-t^*)} E^+. \quad (61)$$

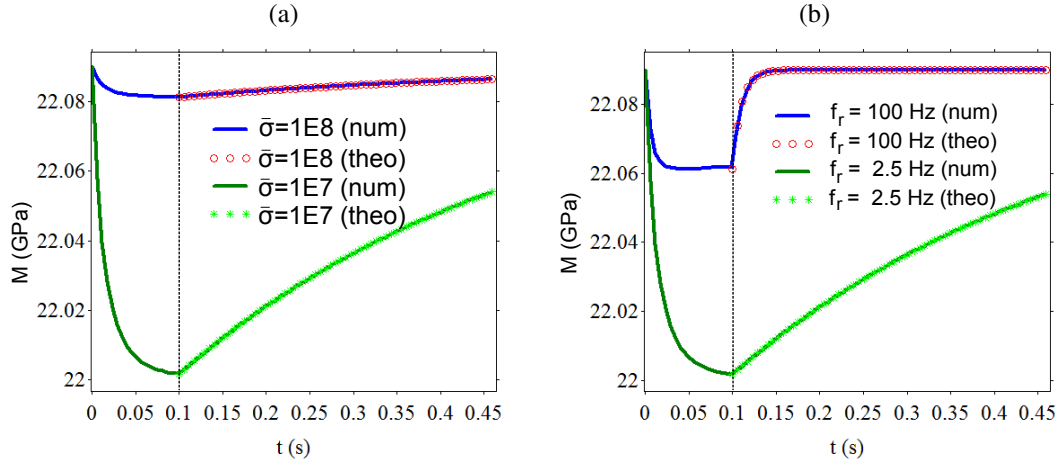


Figure 10: test 3. Time evolution of the elastic modulus M (35) at x_r . (a): influence of the central stress $\bar{\sigma} = 10^8$ Pa and 10^7 Pa. (b): influence of the frequency of restoration $f_r = 2.5$ Hz and 100 Hz. The vertical dotted line denotes the time t^* where the source is switched off.

311 The domain of propagation is $L_x = 0.4$ m long and is discretized onto 100 grid nodes. The
 312 maximal strain is $\varepsilon_{\max} = 10^{-5}$. Time integration is performed during $4 \cdot 10^5$ time steps. Figure 10
 313 shows the time evolution of the elastic modulus $M \equiv E$ (35); this equality occurs only because a
 314 linear stress-strain relation is assumed. The numerical values of M are shown from the beginning
 315 of the simulation, whereas the exact values of E (61) are shown from t^* . For the sake of clarity,
 316 the values are shown only each 5000 time steps. Logically, the elastic modulus decreases as long
 317 as the source is switched on (softening), and then increases up to its initial value (recovering).

318 Figure 10-(a) illustrates the influence of the central stress on the evolution of M : $\bar{\sigma} = 10^8$
 319 Pa or 10^7 Pa (the other parameters are those of table 1). According to the Vakhnenko's ex-
 320 pression (7), these values correspond to spherical defects of radius $2.13 \cdot 10^{-10}$ m and $4.59 \cdot 10^{-10}$
 321 m, respectively. In both cases, equilibrium has been reached at t^* . Lower value of $\bar{\sigma}$ yields a
 322 greater variation of the elastic modulus. This property follows from (9): as $\bar{\sigma}$ decreases, the
 323 curve $g \rightarrow g_\sigma$ stiffens and tend towards a Heaviside step function. Consequently, greater values
 324 of g_σ are obtained when $\bar{\sigma}$ is smaller. It implies a larger evolution of g (5), and hence of E (3).

325 Figure 10-(b) illustrates the influence of the frequency of restoration on the evolution of
 326 M : $f_r = 2.5$ Hz or 100 Hz (the other parameters are those of table 1). The lowest value of
 327 f_r yields a greater variation of the elastic modulus. This is a consequence of the competition
 328 between restoration (with frequency f_r) and destruction (with frequency f_d). When f_r is too low
 329 compared with f_d , restoration has almost no time to occur during one period $T = 1/f_c$, and
 330 destruction plays a preponderant role.

331 5.5. Test 4: full model

332 The fourth and last test incorporates all the physical mechanisms of the model: nonlinear
 333 stress-strain law, viscoelasticity, activation / restoration of defects. The domain is $L_x = 0.4$ m
 334 long and is discretized onto 100 grid nodes. The source is a monochromatic excitation (55).
 335 Time integration is performed during $5 \cdot 10^4$ time steps. The fields are recorded at x_r .

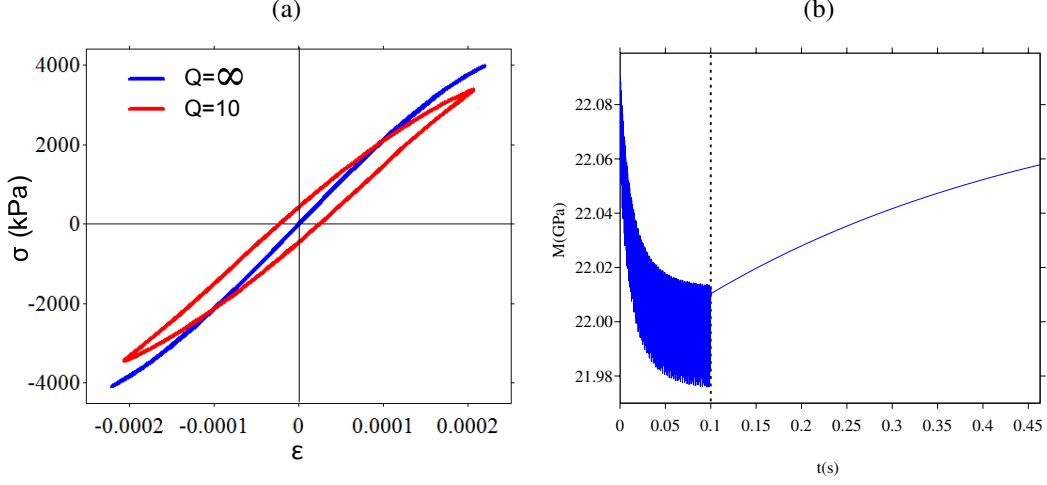


Figure 11: test 4. (a): stress-strain curves at x_r for different quality factor Q and a forcing amplitude $\varepsilon_{\max} = 2.0 \cdot 10^{-4}$. (b): time evolution of the elastic modulus; the vertical dotted line denotes the time t^* where the source is switched off.

336 Figure 11-(a) illustrates the influence of viscoelasticity on the stress-strain law. When viscous
 337 effects are neglected ($Q = +\infty$, where Q is the quality factor), the cubic behavior induced by the
 338 Landau law (15) is observed. Moreover, the scaling (6) induces that the evolution of defects on
 339 one cycle is insufficient to provide a measurable hysteretic effect. On the contrary, hysteresis is
 340 obtained when viscoelasticity is accounted for ($Q = 20$). Figure 11-(b) mimics the simulation of
 341 test 3, where the source is switched-on and off. But unlike test 3, a nonlinear stress-strain relation
 342 is used. One observes large oscillations up to t^* , contrary to figure 10. It reproduces qualitatively
 343 the behavior observed in figure 1.

344 Figure 12 displays the relative variation of the elastic modulus $\Delta M = (M - M_0)/M_0$ in
 345 terms of the strain, for various amplitudes of the forcing. Three observations can be done. First,
 346 nonlinear curves are obtained, which is a signature of the nonlinear stress-strain relation. Second,
 347 ΔM increases with ε_{\max} : softening increases monotonically with the forcing. Third and last,
 348 loops are obtained if and only if viscoelasticity is incorporated (c-d). These three features are
 349 qualitatively similar to those obtained experimentally [15, 16].

350 5.6. Conclusion

351 We have proposed a one-dimensional model that captures the behavior of real media under
 352 longitudinal bar excitation, namely:

- 353 • softening / recovering of the elastic modulus;
- 354 • hysteretic evolution of the elastic modulus with the strain.

355 This model, which extends previous contributions of other authors [19], involves different fre-
 356 quency scales: a fast excitation frequency related to nonlinear elasticity and viscoelastic attenua-
 357 tion, and slow frequencies related to the restoration / destruction of defects. Sound mathematical
 358 properties are ensured: the concentration of defects remains bounded, hyperbolicity is analysed,

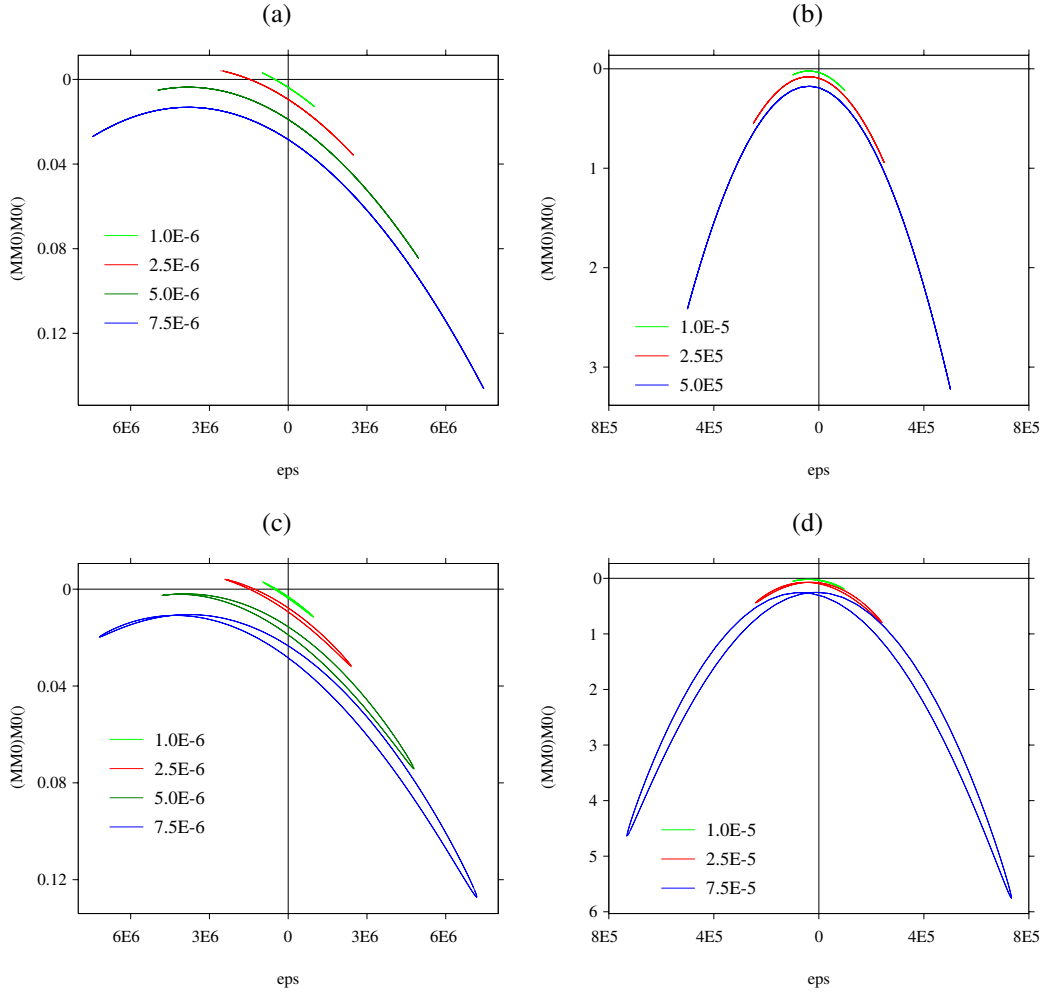


Figure 12: test 4. Relative variations in the elastic modulus M for various amplitudes of forcing ϵ_{\max} , from 10^{-6} to $7.5 \cdot 10^{-5}$. Top (a-b): without viscoelasticity; bottom (c-d): with viscoelasticity.

359 and the energy decreases if the viscoelastic parameters are conveniently determined. Lastly, a ro-
 360 bust numerical scheme has been built. A major interest of the present approach is the possibility
 361 to tackle with variable coefficients in space, which is representative of localized defects [14].

362 Many improvements can be investigated, to cite a few. More sophisticated models can be
 363 built quite naturally, considering for instance relaxation of the nonlinear coefficients \mathbf{p} in (18a),
 364 or a nonlinear law in (18b). Concerning the numerical simulations, higher-order schemes (such as
 365 WENO schemes [10]) may can easily be adapted to the proposed formulation. Lastly, theoretical
 366 analyses should be done to prove rigorously the well-posedness of the model and the decrease of
 367 energy.

368 Two directions of work are currently investigated. First, numerical simulations are done to
 369 recover quantitatively the experimental results of the literature [15, 16]. Second, extension of
 370 this model to 2D-geometries is under progress.

371 Appendix A. Parameters of the viscoelastic model

372 Standard calculations on (16), (18) and (19) yield the reciprocal of the quality factor Q [2]

$$Q^{-1}(\omega) = \left(\sum_{\ell=1}^N \frac{\omega(\tau_{\varepsilon\ell} - \tau_{\sigma\ell})}{1 + \omega^2\tau_{\sigma\ell}^2} \right) / \left(\sum_{\ell=1}^N \frac{1 + \omega^2\tau_{\varepsilon\ell}\tau_{\sigma\ell}}{1 + \omega^2\tau_{\sigma\ell}^2} \right). \quad (\text{A.1})$$

373 Optimizing Q^{-1} towards a given law (for instance a constant quality factor on a frequency range
 374 of interest $[f_{\min}, f_{\max}]$) provides a means to determine $\tau_{\sigma\ell}$ and $\tau_{\varepsilon\ell}$ [12]. Here an optimization
 375 with constraint is applied to ensure positive values of $\tau_{\sigma\ell}$ and $\tau_{\varepsilon\ell}$, as required by the decrease of
 376 energy (see section 3.2). See [3] for details about such an optimization.

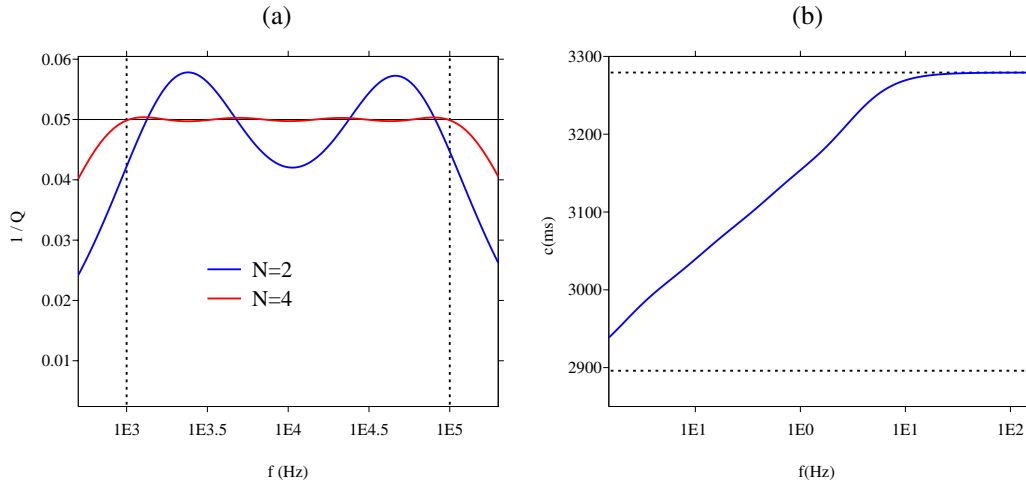


Figure A.13: Properties of the viscoelastic model in the linear regime. (a): reciprocal of the quality factor $Q = 20$ (A.1). The constant exact value is denoted by a horizontal line; the values obtained after optimization with $N = 2$ and $N = 4$ relaxation mechanisms are denoted in blue and red, respectively; the range of optimization $[f_{\min}, f_{\max}]$ is denoted by vertical dotted lines. (b): frequency evolution of the phase velocity; the horizontal dotted lines denote the phase velocity at zero and infinite frequency.

377 Figure A.13 illustrates the properties of the viscoelastic model. Figure A.13-(a) compares
 378 the reciprocal of the constant quality factor $Q = 20$ with the value deduced from (A.1), for $N = 2$
 379 and $N = 4$ relaxation mechanisms. Nonlinear optimization is performed from $f_{\min} = 1$ kHz to
 380 $f_{\max} = 100$ kHz. Large oscillations are obtained for $N = 2$; excellent agreement is observed for
 381 $N = 4$. Figure A.13-(b) shows the increase of phase velocity from $c_0 = \sqrt{E_R/\rho}$ to $c_\infty = \sqrt{E/\rho}$.
 382 The reader is referred to [2] for details about these quantities.

383 Lastly, property 1 is proven here.

384 *Proof.* Null attenuation amounts to an infinite quality factor. Equation (A.1) implies that $Q =$
 385 $+\infty$ is obtained if $\tau_{\varepsilon\ell} = \tau_{\sigma\ell}$. In this case, the viscoelastic coefficients (20) and (21) are

$$E_R = E, \quad K_{1\ell} = \frac{E}{N}, \quad K_{2\ell} = +\infty, \quad \eta_\ell = +\infty. \quad (\text{A.2})$$

386 To get a bounded stress, (18c) implies $\varepsilon_{2\ell} = 0$, and hence $\varepsilon_{1\ell} = \varepsilon$ for $\ell = 1, \dots, N$ (17). Putting
 387 together the total stress (16), the nonlinear elasticity (11) and the homogeneity property in (12),
 388 one obtains

$$\sigma = \sum_{\ell=1}^N s(\varepsilon_{1\ell}, K_{1\ell}, \mathbf{p}) = \sum_{\ell=1}^N s\left(\varepsilon, \frac{E}{N}, \mathbf{p}\right) = \frac{1}{N} \sum_{\ell=1}^N s(\varepsilon, E, \mathbf{p}) = s(\varepsilon, E, \mathbf{p}), \quad (\text{A.3})$$

389 which concludes the proof. \square

390 Appendix B. Proof of property 2

391 The Jacobian \mathbf{A} of \mathbf{f} (31) is

$$\mathbf{A}(\mathbf{U}) = \begin{pmatrix} 0 & 0 & \Phi_1 & \dots & \Phi_N & 0 \\ -1 & 0 & 0 & \dots & 0 & 0 \\ -1 & 0 & 0 & \dots & 0 & 0 \\ \vdots & \vdots & \vdots & & \vdots & \vdots \\ -1 & 0 & 0 & \dots & 0 & 0 \\ 0 & 0 & 0 & 0 & 0 & 0 \end{pmatrix}, \quad (\text{B.1})$$

392 where

$$\Phi_\ell = -\frac{1}{\rho} \frac{\partial \sigma_{1\ell}}{\partial \varepsilon_{1\ell}}. \quad (\text{B.2})$$

393 The determinant of \mathbf{A} writes

$$P_{\mathbf{A}}(\lambda) = -\lambda \begin{vmatrix} -\lambda & 0 & \Phi_1 & \dots & \Phi_N \\ -1 & -\lambda & 0 & \dots & 0 \\ -1 & 0 & -\lambda & & 0 \\ \vdots & & \ddots & \ddots & \\ -1 & & & 0 & -\lambda \end{vmatrix} \quad (\text{B.3})$$

394 The columns and lines are denoted by C_j and \mathcal{L}_j , respectively. The following algebraic manipu-
 395 lations are performed successively:

396 **(i)** $C_1 \leftarrow \lambda C_1$,

397 **(ii)** $C_1 \leftarrow C_1 - C_j$, with $j = 2, \dots, N + 1$,

398 which yields

$$\begin{aligned}
\lambda P_{\mathbf{A}}(\lambda) &= -\lambda \begin{vmatrix} -\lambda^2 - \sum_{\ell=1}^N \Phi_{\ell} & 0 & \Phi_1 & \cdots & \Phi_N \\ 0 & -\lambda & & & \\ \vdots & & & \ddots & \\ 0 & & & & -\lambda \end{vmatrix}, \\
&= (-1)^{N+1} \lambda^{N+2} \left(\lambda^2 + \sum_{\ell=1}^N \Phi_{\ell} \right).
\end{aligned} \tag{B.4}$$

399 It follows the eigenvalues 0 (with multiplicity $N + 1$) and $\pm c$, with the sound velocity (33). From
400 (B.2), real eigenvalues are obtained if and only if the property 2 is satisfied. Given the nonlinear
401 elastic models (13)-(15), the speed of sound c satisfies:

$$c^2 = \begin{cases} \sum_{\ell=1}^N \frac{K_{1\ell}}{\rho} \frac{1}{r-a} \left(\frac{r+1}{\left(1 + \frac{\varepsilon_{1\ell}}{d}\right)^r} - \frac{a+1}{\left(1 + \frac{\varepsilon_{1\ell}}{d}\right)^a} \right) & \text{(model 1),} \\ \sum_{\ell=1}^N \frac{K_{1\ell}}{\rho} \left(1 - (r+a+3) \frac{\varepsilon_{1\ell}}{d} + \frac{1}{2} (r^2 + ra + a^2 + 6r + 6a + 11) \left(\frac{\varepsilon_{1\ell}}{d} \right)^2 \right) & \text{(model 2),} \\ \sum_{\ell=1}^N \frac{K_{1\ell}}{\rho} (1 - 2\beta \varepsilon_{1\ell} - 3\delta \varepsilon_{1\ell}^2) & \text{(model 3).} \end{cases} \tag{B.5}$$

402 Appendix C. Proof of property 3

403 For linear stress-strain relations (18), the relaxation coefficients (32) yield

$$\begin{cases} \frac{\partial \Delta_{\ell}}{\partial \varepsilon}(0) = \frac{1}{\eta_{\ell}} \sigma'_{2\ell}(0) = \frac{K_{2\ell}}{\eta_{\ell}}, \\ \frac{\partial \Delta_{\ell}}{\partial \varepsilon_{1\ell}}(0) = -\frac{1}{\eta_{\ell}} (\sigma'_{1\ell}(0) + \sigma'_{2\ell}(0)) = -\frac{1}{\eta_{\ell}} (K_{1\ell} + K_{2\ell}). \end{cases} \tag{C.1}$$

404 One obtains the Jacobian matrix of the relaxation function (31)

$$\mathbf{J} = \begin{pmatrix} 0 & 0 & \cdots & 0 & 0 \\ \frac{E_{21}}{\eta_1} & -\frac{E_{11} + E_{21}}{\eta_1} & & & 0 \\ \vdots & & \ddots & & \\ \frac{E_{2N}}{\eta_1} & & & -\frac{E_{1N} + E_{2N}}{\eta_N} & 0 \\ 0 & & \cdots & 0 & f_{\xi} \end{pmatrix}, \tag{C.2}$$

405 with $f_{\xi} = f_r$ if $g > g_{\sigma}$, $f_{\xi} = f_d$ if $g < g_{\sigma}$, $f_{\xi} = 0$ else. It follows the eigenvalues 0, $-\frac{K_{1\ell} + K_{2\ell}}{\eta_{\ell}}$, and
406 $-f_{\xi}$.

407 **Appendix D. Semi-analytical solution**

408 The semi-analytical solution of the viscodynamic equations is computed as follows. Fourier
 409 transforms in space and time are applied to the system (56). Applying an inverse Fourier trans-
 410 form in space yields

$$\hat{v}(x, \omega) = \frac{i\omega\rho}{\sum_{\ell=1}^N K_{1\ell} \frac{i\omega + 1/\tau_{\varepsilon\ell}}{i\omega + 1/\tau_{\sigma\ell}}} \frac{\hat{\mathcal{G}}(\omega)}{2\pi} \int_{-\infty}^{+\infty} \frac{1}{k^2 - k_0^2} e^{-ikx_0} dk, \quad (\text{D.1})$$

411 where the hat refers to the Fourier transform, \mathcal{G} is the time evolution of the source, the relaxation
 412 times $\tau_{\varepsilon\ell}$ and $\tau_{\sigma\ell}$ are defined in (19), and k is the wavenumber. The poles $\pm k_0$ satisfy

$$k_0^2 = \frac{\rho\omega^2}{\sum_{\ell=1}^N K_{1\ell} \frac{i\omega + 1/\tau_{\varepsilon\ell}}{i\omega + 1/\tau_{\sigma\ell}}} \quad (\text{D.2})$$

413 with $\Im\text{m}(k_0) < 0$. Applying the residue theorem gives the time-domain velocity

$$v(x, t) = \rho \int_0^{\infty} \Re e \left(\frac{\omega}{k_0} \frac{1}{\sum_{\ell=1}^N K_{1\ell} \frac{i\omega + 1/\tau_{\varepsilon\ell}}{i\omega + 1/\tau_{\sigma\ell}}} e^{-ik_0|x-x_0|} \hat{\mathcal{G}}(\omega) \right) d\omega. \quad (\text{D.3})$$

414 Expressions for ε and $\varepsilon_{1\ell}$ can be obtained in a similar manner. Lastly, the numerical evaluation of
 415 (D.3) is done by a rectangular quadrature rule on N_f Fourier modes and with a constant frequency
 416 step Δf on the frequency band of interest.

- 417 [1] J. D. ACHENBACH, *Wave Propagation in Elastic Solids*, North-Holland Publishing, Amsterdam (1973).
 418 [2] J. M. CARCIONE, *Wave Fields in Real Media: Wave Propagation in Anisotropic, Anelastic, Porous and Electromag-*
 419 *netic Media*, Elsevier (2007).
 420 [3] A. BEN JAZIA, B. LOMBARD, C. BELLIS, *Wave propagation in a fractional viscoelastic Andrade medium: diffusive*
 421 *approximation and numerical modeling*, *Wave Motion*, 51 (2014), 994-1010.
 422 [4] S. F. DAVIS, *Simplified second-order Godunov-type methods*, *SIAM J. Sci. Stat. Comput.*, 9 (1988), 445-473.
 423 [5] R. A. GUYER, P. A. JOHNSON, *Nonlinear mesoscopic elasticity: Evidence for a new class of materials*, *Physics*
 424 *Today* 52 (1999), 30-35.
 425 [6] R. A. GUYER, P. A. JOHNSON, *Nonlinear Mesoscopic Elasticity: The Complex Behaviour of Rocks, Solis, Concrete*,
 426 *Wiley* (2009).
 427 [7] M. F. HAMILTON, D. T. BLACKSTOCK, *Nonlinear Acoustics*, Academic Press (1998).
 428 [8] P. A. JOHNSON, B. ZINSZNER, P. N. J. RASOLOFOSON, *Resonance and elastic nonlinear phenomena in rock*, *J. Geo-*
 429 *phys. Res.*, 101 (1996), 11553-11564.
 430 [9] L. LANDAU, E. LIFSHITZ, *Theory of Elasticity*, Pergamon Press (1970).
 431 [10] R. J. LEVEQUE, *Finite Volume Methods for Hyperbolic Problems*, Cambridge University Press (2002).
 432 [11] R. J. LEVEQUE, D. H. YONG, *Solitary waves in layered nonlinear media*, *SIAM J. Appl. Math.*, 63-5 (2003), 1539-
 433 1560.
 434 [12] B. LOMBARD, J. PIRAUX, *Numerical modeling of transient two-dimensional viscoelastic waves*, *J. Comput. Phys.*,
 435 230-15 (2011), 6099-6114.
 436 [13] S. NDANOU, N. FAVRIE, S. GAVRILYUK, *Criterion of hyperbolicity in hyperelasticity in the case of the stored energy*
 437 *in separable form*, *J. Elast.*, 115 (2014), 1-25.

- 438 [14] C PECORARI, D.A. MENDELSON, *Forced nonlinear vibrations of a one-dimensional bar with arbitrary distributions*
439 *of hysteretic damage*, to appear in J. Nondestruct. Eval. (2014).
- 440 [15] G. RENAUD, P.Y. LE BAS, P.A. JOHNSON, *Revealing highly complex elastic nonlinear (anelastic) behavior of Earth*
441 *materials applying a new probe: Dynamic acoustoelastic testing*, J. Geophys. Res., 117 (2012), B06202.
- 442 [16] J. RIVIERE, G. RENAUD, R.A. GUYER, P.A. JOHNSON, *Pump and probe waves in dynamic acousto-elasticity: Compre-*
443 *hensive description and comparison with nonlinear elastic theories*, J. Appl. Phys., 114 (2013), 054905.
- 444 [17] J.A. TEN CATE, T.J. SHANKLAND, *Slow dynamics in the nonlinear elastic response of Berea sandstone*, Geophys.
445 Res. Lett., 23-21 (1996), 3019-3022.
- 446 [18] E.F. TORO, *Riemann Solvers and Numerical Methods for Fluid Dynamics. A Practical Introduction*, Springer-
447 Verlag (1999).
- 448 [19] O. O. VAKHNENKO, V. O. VAKHNENKO, T. J. SHANKLAND, *Soft-ratchet modeling of end-point memory in the nonlinear*
449 *resonant response of sedimentary rocks*, Physical Review B71 (2005), 174103.